Optics Letters

Integrated heterodyne interferometer with on-chip modulators and detectors

David B. Cole,[1] Cheryl Sorace-Agaskar,[1] Michele Moresco,[1] Gerald Leake,[2] Douglas Coolbaugh,[2] and Michael R. Watts[1,*]

[1]Research Laboratory of Electronics, Massachusetts Institute of Technology, Cambridge, Massachusetts 02139, USA
[2]College of Nanoscale Science and Engineering, University at Albany, Albany, New York 12203, USA
*Corresponding author: mwatts@mit.edu

Received 26 March 2015; revised 5 June 2015; accepted 8 June 2015; posted 9 June 2015 (Doc. ID 236841); published 25 June 2015

We demonstrate, to our knowledge, the first on-chip heterodyne interferometer fabricated on a 300-mm CMOS compatible process that exhibits root-mean-square (RMS) position noise on the order of 2 nm. Measuring 1 mm by 6 mm, the interferometer is also, to our knowledge, the smallest heterodyne interferometer demonstrated to date and will surely impact numerous interferometric and metrology applications, including displacement measurement, laser Doppler velocimetry and vibrometry, Fourier transform spectroscopy, imaging, and light detection and ranging (LIDAR). Here we present preliminary results that demonstrate the displacement mode.

OCIS codes: (060.2840) Heterodyne; (120.3180) Interferometry; (120.7250) Velocimetry; (250.5300) Photonic integrated circuits; (280.3340) Laser Doppler velocimetry; (280.3640) Lidar.

http://dx.doi.org/10.1364/OL.40.003097

The application of CMOS processing techniques developed in the microelectronics world to that of silicon photonics has been the catalyst for the rapid proliferation of smaller, higher performance, and more densely integrated photonic devices that are rapidly advancing the field with large-scale implementations of photonic micro-systems. A recent example is the Sun *et al.* [1] demonstration of a 64 × 64 optical phased array, a device that highlights the integration possible with silicon photonics.

Moreover, this advanced 300-mm silicon photonics platform has led to a number of demonstrations including ultra-low power silicon modulators [2], rapid, wide-angle-steered phased arrays [3], and integrated single-sidebands modulators (SSBMs), to name a few. It is only logical that as the silicon photonics library continues to grow, these devices will be synthesized into complete photonic systems for applications including optical networking and communications, imaging, and sensors. Among complex optical systems, the interferometer represents perhaps the most important class of optical sensors and scientific instruments ever developed. Since the famous work of Michelson, the interferometer has become one of the most important scientific instruments. Today, interferometric techniques are key to applications such as displacement measurement, laser Doppler vibrometry/velocimetry, Fourier transform spectroscopy, optical surface characterization, and LIDAR.

Importantly, interferometers are crucial for lithography and high-precision semiconductor manufacturing [4]. In these critical applications, the preferred operational mode is the heterodyne interferometer, where displacement is manifested as a phase difference between a pair of equal frequency sinusoids. This is in contrast to the less-sensitive and more error-prone amplitude measurement common to traditional homodyne interferometers.

However, modern heterodyne interferometers are complex optical systems requiring bulk beam-splitters, waveplates, and frequency modulators to be implemented. As a result, they are large and expensive precision instruments that are limited to industrial and scientific applications. The development of a chip-scale integrated interferometer, with its significantly smaller form factor, increased stability, and lower cost, can greatly expand the application of interferometry to automobiles and handheld medical and consumer devices.

Leveraging silicon photonics, all the required components can be realized on-chip, allowing for a low-cost, chip-scale, high-precision interferometer to be implemented. In this Letter, we present the design and experimental results of the first silicon-chip-scale heterodyne interferometer. The device is constructed of a series of on-chip beam-splitters, SSBMs, and germanium (Ge) detectors configured in a Michelson-like configuration. It achieves an RMS position noise of ~2 nm, defined as the standard deviation of the measured position, in a 1 mm by 6 mm footprint. We begin by reviewing the theory, then describe the device and experiment before closing with preliminary results.

Dahlquist *et al.* [5] first applied heterodyning techniques to interferometry in 1966 by using the Zeeman split of a He–Ne laser to generate two frequencies with orthogonal polarizations.

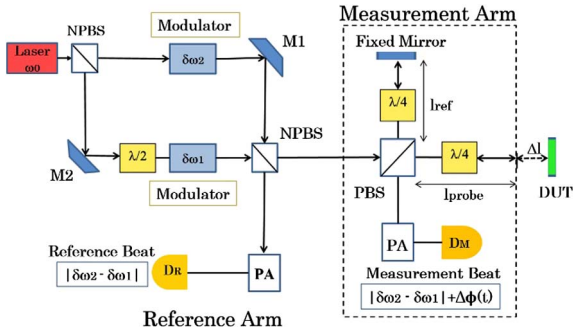

Fig. 1. Bulk heterodyne interferometer.

Because traditional bulk interferometers are free space, the two frequency beams defining the measurement and reference arms must be spatially separated until collinearly combined at the detectors. This is accomplished with optical components such as non-polarizing beam splitters (NPBS), polarizing beam splitters (PBS), polarization analyzers (PA), and waveplates as shown in Fig. 1. The use of bulk components therefore limits scalability.

While this is the first such device developed in silicon, on-chip heterodyne interferometers on $LiNbO_3$ [6,7] have previously been demonstrated. The device developed by Toda *et al.*, measuring 47 mm by 5 mm, achieved a resolution of ±3 nm at a wavelength of 633 nm. The heterodyne frequencies were generated using an on-chip mode converter and phase modulator. However, the detectors were external to the device. Because both frequencies were generated concurrently by a single modulator, they were separated by utilizing orthogonal TE and TM modes. Therefore, on-chip mode converters, mode splitters, and polarizers are required, similar to bulk interferometers. An external quarter waveplate is also required to rotate the outgoing TM wave to TE upon reflection to allow interference between the reference and measurement signals.

Our proposed device is shown below in Fig. 2. Because the heterodyne tones are generated separately, silicon waveguides rather than bulk optics maintain spatial separation, allowing the size to be significantly reduced.

A laser of frequency ω_0 and TE polarization is split between two SSBMs, which modulate their respective outputs to ω_1 and ω_2 (3a and 3b). The output of each SSBM is further divided by a 50:50 splitter with half the power from each incident on a

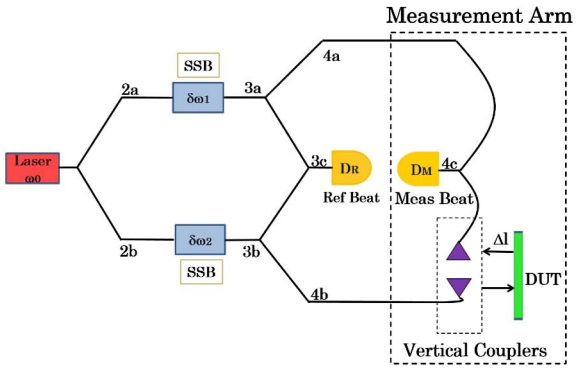

Fig. 2. Integrated heterodyne interferometer.

pair of Ge detectors operated in a balanced mode. Unlike single detector systems, where only half the available power is collected, balanced detection captures an additional 3 dB with the added benefit of removing the DC intensity components [8,9]. Theoretically, any common-mode noise that limits detector sensitivity can be eliminated, and balanced detection has been shown to remove a considerable portion of amplitude-modulation noise [10,11]. The adiabatic splitters, measuring 150 μm in length, have a sum-difference (180°-hybrid) transfer function given by

$$T_{\Sigma,\Delta} = \begin{bmatrix} \frac{1}{\sqrt{2}} & \frac{1}{\sqrt{2}} \\ -\frac{1}{\sqrt{2}} & \frac{1}{\sqrt{2}} \end{bmatrix}. \tag{1}$$

Therefore, one output sums the incident fields, while the other gives the difference, which is well-suited to balanced detection. We designate the first detector pair, shown at 3c in Fig. 2, as the reference pair. These are used to calibrate the input phase of the interferometer, enabling spurious drifts to be removed. If we designate the detector coincident with the sum port as the sum detector and the other the difference detector, the respective electric fields can be written as

$$E_\Sigma = \frac{1}{\sqrt{2}}(E_{\text{Upper}} + E_{\text{Lower}}), \tag{2}$$

$$E_\Delta = \frac{1}{\sqrt{2}}(-E_{\text{Upper}} + E_{\text{Lower}}). \tag{3}$$

Expressing the electric fields from the SSBMs (3a and 3b) into the reference path as

$$E_{\text{Upper}} = E_1 e^{-j(\omega_1 t+\phi_1)}, \tag{4}$$

$$E_{\text{Lower}} = E_2 e^{-j(\omega_2 t+\phi_2)}, \tag{5}$$

the electric fields and intensities at the sum and difference ports of the reference detectors can be written as

$$E_\Sigma = \left[\frac{E_2}{\sqrt{2}} e^{-j(\omega_2 t+\phi_2)} + \frac{E_1}{\sqrt{2}} e^{-j(\omega_1 t+\phi_1)}\right], \tag{6}$$

$$E_\Delta = \left[\frac{E_2}{\sqrt{2}} e^{-j(\omega_2 t+\phi_2)} - \frac{E_1}{\sqrt{2}} e^{-j(\omega_1 t+\phi_1)}\right], \tag{7}$$

$$I_\Sigma \propto \frac{|E_1|^2}{2} + \frac{|E_2|^2}{2} + E_1E_2\cos((\omega_2-\omega_1)t + (\phi_2-\phi_1)), \tag{8}$$

$$I_\Delta \propto \frac{|E_1|^2}{2} + \frac{|E_2|^2}{2} - E_1E_2\cos((\omega_2-\omega_1)t + (\phi_2-\phi_1)). \tag{9}$$

Assuming an equal responsivity R for each detector, the balanced photocurrent from the reference pair is given by

$$i_{\text{Reference}} = i_\Sigma - i_\Delta \propto 2\mathcal{R}\sqrt{I_1 I_2}\cos(\omega_{\text{IF}} t + \delta\phi), \tag{10}$$

where the frequency difference $\omega_2 - \omega_1$ in Eq. (10) is written as ω_{IF}, the intermediate frequency (IF) formed from the heterodyne mixing. The initial phase difference $(\phi_2 - \phi_1)$ in the reference pair is written $\delta\phi$, and the electric field amplitudes

E_1 and E_2 are given in terms of their respective intensities. The remaining signal from the upper SSBM is directed into what is the functional equivalent of the bulk interferometer's reference arm (4a). The remaining signal from the lower SSBM (4b) is edge-coupled off-chip, collimated, and reflected from a corner cube reflector (CCR) mounted to a nanopositioner. The reflected measurement signal is coupled back into a separate waveguide where it combines with the reference arm signal. We assume the incident fields at (4c) are given by

$$E_{\text{Reference}} = E_R e^{-j(\omega_1 t+\phi_R)}, \tag{11}$$

$$E_{\text{Measurement}} = E_M e^{-j(\omega_1 t+\phi_M)}. \tag{12}$$

These form a photocurrent in the measurement detectors given by

$$i_{\text{Measurement}} \propto 2\mathcal{R}\sqrt{I_R I_M}\,\cos(\omega_{\text{IF}} t + \phi_R - \phi_M). \tag{13}$$

If the position of the CCR changes by a one-way distance Δd, the measurement signal is shifted in phase with respect to the reference signal by

$$\Delta\phi_M = 4\pi\frac{\Delta d}{\lambda}, \tag{14}$$

where λ is the optical wavelength of the measurement signal in the propagation medium. It is this phase shift that allows the relative displacement to be measured.

Our device, shown in Fig. 3, was fabricated on a 300-mm CMOS compatible Silicon on Insulator (SOI) process using 193-nm optical immersion lithography and measures approximately 1 mm by 6 mm.

The optical modulation is provided by two SSBMs, shown conceptually in Fig. 4. Each SSBM measures ~2 mm in length and consists of two Mach–Zehnder (MZ) phase modulators operated in push-pull. Within a SSBM, the phase modulators share a common DC bias voltage, but are driven by RF signals in phase quadrature. When operated in this manner, the frequency of the input is shifted by an amount equal to the RF signal such that

$$\omega_{\text{Modulated}} = \omega_0 \pm \omega_{\text{RF}}. \tag{15}$$

Total insertion loss is estimated to be ~7 dB for the unsuppressed carrier, and the 3-dB frequency was measured to be 10 GHz. Single-sideband operation at 1.55 μm shows more than 18-dB carrier suppression and more than 15-dB spurious sideband suppression. Whether the upper or lower sideband is obtained depends on the relative bias between the upper and lower arms. Thus suppression of the carrier and unwanted sideband is sensitive to the relative phase between the phase shifters. Due to fabrication tolerances, each modulator must be calibrated to achieve the correct phase relationships. Phase compensation is accomplished using three thermo-optic heaters residing in the MZ arms. In total, each SSBM requires six control voltage: 2 RF, 1 DC bias, and 3 heaters biases. The Ge detectors, similar to one described in [12], measure 1.2 μm wide by 10 μm in length, with a 800-nm Ge trench. The measured responsivity at 1.55 μm is approximately 0.5 A/W. The SSBM and detector sections are shown in Fig. 5.

The measurement and reference photocurrents are converted to voltages via transimpedance amplifiers (TIAs).

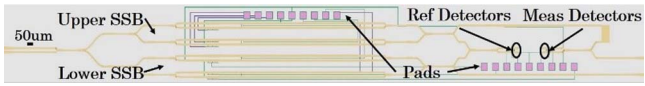

Fig. 3. Integrated heterodyne interferometer.

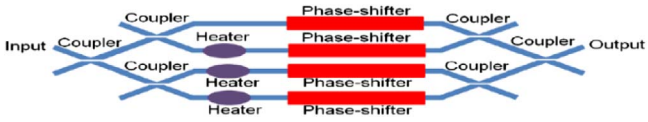

Fig. 4. Single-sideband modulator (SSBM).

This produces two voltage waveforms with the same frequency ω_{IF}, but in general different phases. The TIA outputs are bandpass filtered then sampled by a high-speed oscilloscope, which is controlled from a PC-based MATLAB script to save the data for analysis. Figure 6 shows the measurement voltage for several CCR displacements.

The measurement signal is compared to the reference signal and the phase is recovered via quadrature demodulation. For this, a copy of the reference signal is digitally shifted 90° using a Hilbert transform, converting a cosine into a sine or vice versa. The reference signal cosine and sine images each multiply a copy of the measurement signal. This produces in-phase (I) and quadrature (Q) components at baseband and $2f_{\text{IF}}$. The high-frequency terms are removed using a FIR low-pass filter and the phase is recovered by

$$\phi = \arctan\frac{Q}{I}. \tag{16}$$

Because the arctangent is modulo 2π, the phase shift has an ambiguous length of $\lambda/2$. The minimum detectable phase shift, and hence the minimum displacement, is limited primarily by system noise and ambient vibrations. A nanopositioner with 0.5-nm RMS position noise and 100-ppm accuracy over a

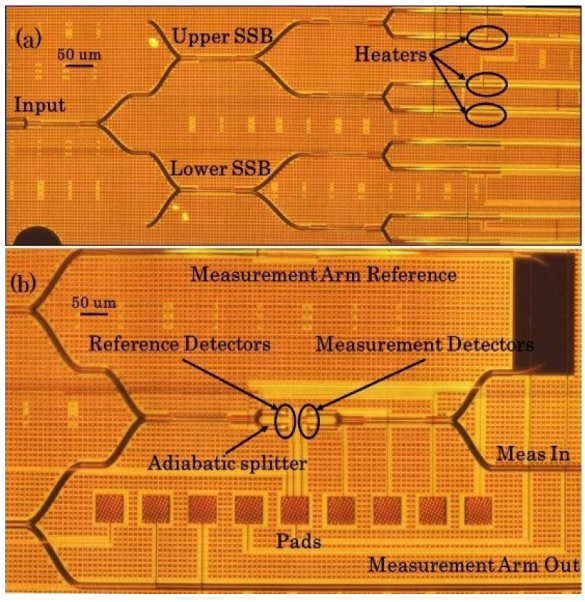

Fig. 5. (a) SSBM and (b) detector sections.

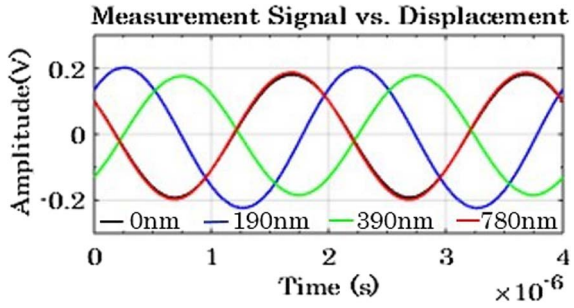

Fig. 6. Measurement signal versus displacement.

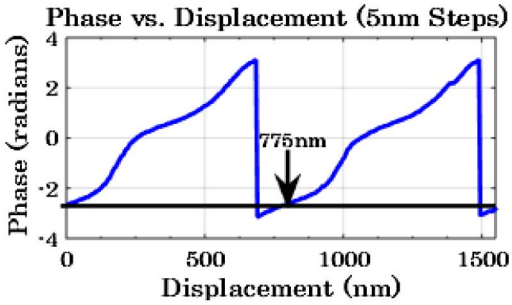

Fig. 7. Wrapped phase versus displacement.

100-μm range was displaced in 5-nm steps from zero to 1.55 μm, with the wrapped phase shown in Fig. 7. The phase ambiguity occurs at 775 nm as expected. However, we also notice a periodic modulation of the ideally linear phase. This modulation, more commonly known as a nonlinearity [4,13–15], is caused by frequency leakage between the two SSBMs. The nonlinearity was corrected by deriving the equations of the ellipse described by the IQ components. By plotting Q versus I, we obtain the well-known Lissajous curves, which are shown in Fig. 8 as the CCR was displaced ±2 μm by a 50-Hz triangular wave. The nonlinearity causes a non-zero eccentricity of the ellipse and a shift of the center away from the origin. By fitting the IQ data using least squares methods, we can "circularize" the ellipse and reduce the nonlinearity as shown in Fig. 8.

Table 1 summarizes the results of stepping the CCR from zero to 1.55 μm in steps of 5, 10, and 25 nm, respectively. The corrected measurements show a marked improvement in the position variance, and hence the RMS position noise.

In this Letter we have demonstrated an integrated heterodyne interferometer on silicon with on-chip splitters, modulators, and detectors that obtains a RMS position noise of ~2 nm. Compared to conventional interferometers based on bulk optics, this chip-scale device offers significant reduction in size and cost, as well as increased stability due to the CMOS-compatible silicon photonic integration, thus creating opportunities for applications in 3D inspection, automotive, handheld devices, and portable biomedical units.

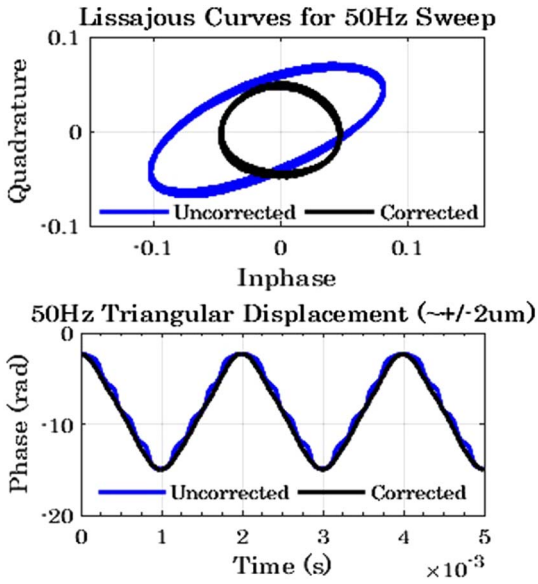

Fig. 8. Lissajous curves and phase for uncorrected and corrected 50-Hz triangle-wave displacement.

Table 1. Summary of Stepped Measurements

	Uncorr Avg	Uncorr Std	Corrected Avg	Corrected Std
5 nm	4.94	3.56	4.88	2.52
10 nm	9.91	5.16	9.87	2.19
25 nm	25.04	11.76	25.07	2.36

REFERENCES

1. J. Sun, E. Timurdogan, A. Yaacobi, E. S. Hosseini, and M. R. Watts, Nature **493**, 195 (2013).
2. M. R. Watts, in *Photonics in Switching Conference* (Optical Society of America, 2014), p. JT2B-2.
3. A. Yaacobi, J. Sun, M. Moresco, G. Leake, D. Coolbaugh, and M. R. Watts, Opt. Lett. **39**, 4575 (2014).
4. N. Bobroff, Appl. Opt. **26**, 2676 (1987).
5. J. A. Dahlquist, D. G. Peterson, and W. Culshaw, Appl. Phys. Lett. **9**, 181 (1966).
6. H. Toda, M. Haruna, and H. Nishihara, J. Lightwave Technol. **9**, 683 (1991).
7. A. Rubiyanto, H. Herrmann, R. Ricken, F. Tian, and W. Sohler, J. Nonlinear Opt. Phys. Mater. **10**, 163 (2001).
8. S. Alexander, J. Lightwave Technol. **5**, 523 (1987).
9. B. L. Kasper, C. A. Burrus, J. R. Talman, and K. L. Hall, Electron. Lett. **22**, 413 (1986).
10. C. Davis, Nucl. Phys. B Proc. Suppl. **6**, 290 (1989).
11. J. Shapiro, IEEE J. Quantum Electron. **21**, 237 (1985).
12. C. T. DeRose, D. C. Trotter, W. A. Zortman, A. L. Starbuck, M. Fisher, M. R. Watts, and P. S. Davids, Opt. Express **19**, 24897 (2011).
13. S. J. A. G. Cosijns, H. Haitjema, and P. H. J. Schellekens, Precis. Eng. **26**, 448 (2002).
14. C. Sutton, J. Phys. E. **1290**, 2 (2000).
15. T. Eom, T. Choi, K. Lee, H. Choi, and S. Lee, Meas. Sci. Technol. **13**, 222 (2002).